

RESEARCH

A Fast Image Simulation Algorithm for Scanning Transmission Electron Microscopy

Colin Ophus

Abstract

Image simulation for scanning transmission electron microscopy at atomic resolution for samples with realistic dimensions can require very large computation times using the existing simulation algorithms. We present a new algorithm that combines features of the two most commonly used algorithms, the Bloch wave and multislice methods. We show that in many cases this algorithm, called PRISM, can provide two or more orders of magnitude speed up over the multislice method with negligible error. We demonstrate the usefulness of this method with large-scale image simulation of a crystalline nanoparticle on an amorphous substrate, varying the detector geometry, probe convergence angle, defocus of the probe and sample tilt.

Keywords: Scanning Transmission Electron Microscopy; Electron Scattering; Image Simulation

Introduction

Transmission electron microscopy (TEM) is one of the most versatile and powerful experimental tools for imaging and diffraction of micrometer to sub-nanometer structures. The recent widespread adoption of hardware aberration correction has in particular enabled routine atomic resolution imaging of structures [1–3]. A more recent technical advance for TEM experiments is the use of direct electron detectors (DEDs). These cameras have a much higher quantum efficiency than standard charge-coupled devices with a scintillator, and can also operate at much higher speeds [4–7]. Direct electron detectors have already created dramatic improvements in plane-wave TEM imaging

experiments, especially single-particle biological cryo-EM studies [8–10]. These detectors have also enabled many new kinds of experiments for scanning transmission electron microscopy (STEM), where the electron probe is converged to very small dimensions and scanned across the surface of a sample, because the camera speed is high enough to record a full image of the diffracted probe at each probe position [11]. Examples include nanobeam electron diffraction strain measurements [12, 13], orientation mapping of semi-crystalline polymers [14], and phase contrast imaging modes such as differential phase contrast [15], phase plate interferometry [16], and ptychography [17].

However, while the experimental capabilities of TEM and STEM have expanded, simulation methods have remained largely unchanged for some time. The two primary methods currently used for atomic-resolution simulations are Bloch wave calculations and the multislice method [18]. In the Bloch wave method, the electron wavefunction is defined using a basis set that satisfies the Schrödinger equation inside the sample. After calculating the eigenvectors and eigenvalues of this basis set, the wavefunction at the entrance surface of the sample can be matched to the known electron probe coefficients, and then the resulting electron wavefunction can be computed everywhere (including the exit surface of the sample) [19, 20]. This scattering calculation can be written compactly in a scattering matrix (often called the S-matrix) formalism [18]. Bloch wave calculations are almost never used for imaging or diffraction simulations of large samples (beyond the several ‘unit cell’ scale for crystalline materials) for two reasons; the first is that eigendecomposition of a non-sparse Bloch wave matrix large enough to accurately simulate image sizes $\geq 1000^2$ pixels would take an impractically long time to compute. The second is that the storage requirements of this scale of S-matrix is greater than a terabyte, and using it would require trillions of multiplication operations [18].

A more efficient formulation for large electron scattering simulations is the multislice algorithm [21]. In this method, the atoms of the simulated sample are divided up into infinitely thin slices along the beam direction. The resulting electron scattering is calculated by alternating between a transmission operator

Correspondence: cophus@gmail.com

National Center for Electron Microscopy, Molecular Foundry, Lawrence Berkeley National Laboratory, 1 Cyclotron Road, Berkeley, USA
Full list of author information is available at the end of the article

through each slice, followed by Fresnel propagation of the electron wave to the next slice. These operations can be performed efficiently in realspace and reciprocal space respectively, and so an efficient implementation of this method requires a forward and inverse Fourier transform at each step [18]. The multislice algorithm is very efficient for plane-wave, conventional TEM image or diffraction simulations. It is much less efficient for STEM simulations consisting of thousands or millions of probe positions. This is because while the atomic scattering potential can be reused for all probe positions, the transmission and propagation steps must be repeated for each additional probe position. The scattering potential calculations can be performed very efficiently using look-up tables [16, 22] or a point scattering method [23], but the slow part of the calculation is usually repeated for all probe positions [18]. Many STEM studies, such as those using atomic electron tomography [24, 25], require hundreds of image simulations of many thousands of STEM probe positions, which requires long computation times even with modern implementations of the multislice method [23, 26–29]. It is therefore desirable to develop an electron scattering simulation algorithm that shares the calculation burden between STEM probe positions in a more efficient manner than multislice simulation.

In this manuscript, we derive a more efficient algorithm for STEM simulations by combining aspects of the multislice and Bloch wave methods. We use the multislice method to directly calculate a subset of the rows of the **S**-matrix (corresponding to plane waves of various orientations), which is then used in a similar manner as Bloch wave calculations to relate the output wavefunction to a given input. The key insight is that because highly-converged STEM probes decay to zero quickly with distance from the probe center position, they can be cropped out of the full **S**-matrix in a highly-accurate Fourier interpolation scheme. The algorithm presented here is referred to as the plane-wave reciprocal-space interpolated scattering matrix (PRISM) algorithm. We also compare the accuracy and computation time of the PRISM and multislice algorithms, and demonstrate some useful extensions of the PRISM method including simulating electron probe tilt, probe defocus and changing probe convergence angle.

Theory and Methods

The Multislice and Bloch Wave Methods

For previously published TEM simulation methods, we will briefly outline the required steps here. We refer readers to Kirkland for more information on these

methods [18]. We will also only describe the scattering of the electron beam while passing through a sample; probe-forming optics and the microscope transfer function mathematics are described in many other works. All elastic scattering TEM simulations aim to describe how an electron wavefunction $\psi(\vec{r})$ evolves over the 3D coordinates $\vec{r} = (x, y, z)$. The evolution of the slow-moving portion of the wavefunction along the optical axis z can be described by the Schrödinger equation for fast electrons [18]

$$\frac{\partial\psi(\vec{r})}{\partial z} = \frac{i\lambda}{4\pi}\nabla_{xy}^2\psi(\vec{r}) + i\sigma V(\vec{r})\psi(\vec{r}), \quad (1)$$

where λ is the relativistic electron wavelength, ∇_{xy}^2 is the 2D Laplacian operator, σ is the relativistic beam-sample interaction constant and $V(\vec{r})$ is the electrostatic potential of the sample.

The Bloch wave method uses a basis set that satisfies Eq. 1 everywhere inside the sample boundary, which is assumed to be periodic in all directions. This basis set is calculated by calculating the Eigendecomposition of a set of linear equations that approximate Eq. 1 up to some maximum scattering vector $|k_{\max}|$. Then, for each required initial condition such as different STEM probe positions on the sample surface, we compute the weighting coefficients for each element of the Bloch wave basis set. Finally, the exit wave after interaction of the sample is calculated by multiplying these coefficients by the basis set. This procedure can be written in terms of a scattering matrix **S** as [18]

$$\psi_f(\vec{r}) = \mathbf{S} \psi_0(\vec{r}), \quad (2)$$

where $\psi_0(\vec{r})$ and $\psi_f(\vec{r})$ are the incident and exit wavefunctions respectively. The Bloch wave method can be extremely efficient for very small simulations, where the field of view is on the scale of crystalline unit cells. High symmetry is also an asset for Bloch wave simulations, as we can limit the beam of plane waves (beams) included in the basis set to a small number. However, for a large STEM simulation consisting of thousands or even millions of atoms in the simulation, the **S**-matrix may contain billions or even trillions of entries, which requires an impractical amount of computation time to determine the Eigendecomposition. And actually using Eq. 2 many times for various electron proves will also take far too long. Thus Bloch wave methods are typically only used for very small size STEM simulations.

The most commonly employed method for large STEM simulations is the multislice algorithm. The multislice method alternates between solving the two terms on the right hand side of Eq. 1 individually, for

thin slices of thickness t taken from the sample. The left term is interpreted as a Fresnel propagation operator, which can be efficiently applied in Fourier space as [18]

$$\Psi_{p+1}(\vec{q}) = \Psi_p(\vec{q}) \exp(-i\pi\lambda|\vec{q}|^2t) \quad (3)$$

where $\Psi(\vec{q}) = \mathcal{F}\{\psi(r)\}$ is the Fourier transform of $\psi(\vec{r})$, $\vec{q} = (q_x, q_y)$ is the 2D coordinate vector for Fourier space, and the subscript p refers to the slice index. The second operator of Eq. 1 can be efficiently applied in real space as

$$\psi_{p+1}(\vec{r}) = \psi_p(\vec{r}) \exp[i\sigma V_p^{2D}(\vec{r})], \quad (4)$$

where $V_p^{2D}(\vec{r})$ is the 2D electrostatic potential of all atoms inside slice p , integrated over the slice along the beam direction from the 3D potential. In practice, the atomic potentials are integrated into 2D potentials before the simulation, and then added directly to the slice potential, or applied using convolution [23]. These two steps describe how the electron wavefunction evolves slice-by-slice until it has interacted with the entire sample, applied sequentially as

$$\psi_{p+1}(\vec{r}) = \mathcal{F}^{-1} \left\{ \mathcal{F} \left\{ \psi_p(\vec{r}) e^{i\sigma V_p^{2D}(\vec{r})} \right\} e^{-i\pi\lambda|\vec{q}|^2t} \right\}, \quad (5)$$

where $\mathcal{F}^{-1}\{\cdot\}$ is the inverse Fourier transform. The Multislice method is simple to implement and very accurate, but is not very efficient for large scale STEM simulation. The reason is that although the atomic potentials can be re-used for different probe positions, the remainder of the calculation (using Eq. 5 to propagate each probe through the sample) must be run independently. While this problem is amenable to parallelization, none of the calculations are shared between different probe positions, or different probe parameters such as defocus, convergence angle or probe tilt. In the next section, we will show how a STEM simulation can be reformulated into an S-matrix approach, where the computational load of applying Eq. 5 can be shared between different probe configurations.

The PRISM Algorithm for STEM Simulations

The first step is to separate all atomic coordinates of the simulation cell (which is assumed to be orthorhombic here) into slices, shown in Fig. 1a. These slices can have unequal thickness to better match the atomic coordinates, but should not have thicknesses larger than the average atomic spacing as this could cause errors [18]. The second step is to calculate the 2D projected potentials $V(\vec{r})$ for all slices, as in Fig. 1b.

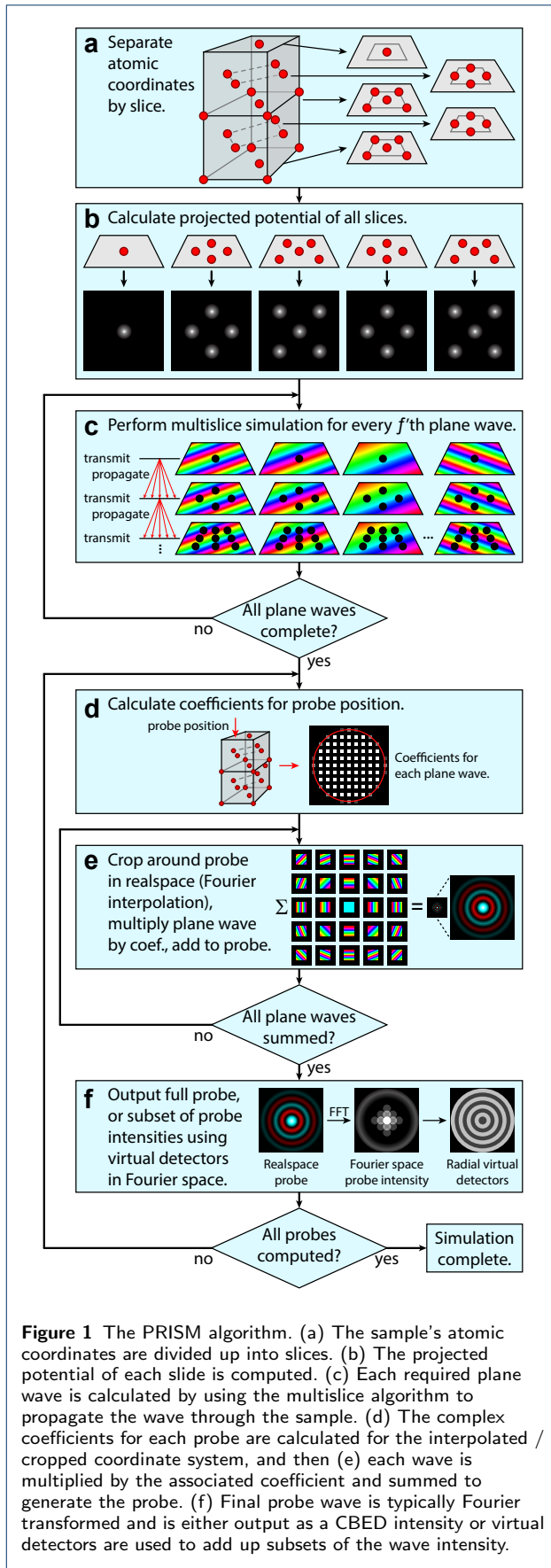


Figure 1 The PRISM algorithm. (a) The sample's atomic coordinates are divided up into slices. (b) The projected potential of each slice is computed. (c) Each required plane wave is calculated by using the multislice algorithm to propagate the wave through the sample. (d) The complex coefficients for each probe are calculated for the interpolated / cropped coordinate system, and then (e) each wave is multiplied by the associated coefficient and summed to generate the probe. (f) Final probe wave is typically Fourier transformed and is either output as a CBED intensity or virtual detectors are used to add up subsets of the wave intensity.

Next, we choose an interpolation factor f . In practice a different factor can be used in x and y , but for simplicity we will describe the simulation method for a square (in the (x, y) plane) simulation cell of size d . This factor f should be chosen to be large enough so that a square area with a side length of the simulation cell size divided by f can encompass all possible STEM probes after they pass through the cell. This can be estimated by numerically simulating a few probes using the conventional multislice method or the method described here. We then also choose a maximum incident probe semi-angle α_{\max} . Note that the simulation will include larger scattering angles than this value, and that this value should be equal to the largest desired probe semiangle plus f times the Fourier space pixel size Δq . We then determine a set of plane wave initial conditions to simulate using the multislice method, shown in Fig. 1c. This set of plane waves corresponds to the incident electron probe

$$\Psi_{m,n}(\vec{q}) = \delta(q_x - mf\Delta q, q_y - nf\Delta q), \quad (6)$$

where $\sqrt{m^2 + n^2}f\lambda\Delta q \leq \alpha_{\max}$, $\delta(\vec{q})$ is the delta function, and (m, n) are integers representing the plane wave index. Thus, we compute only a subset of all possible periodic plane waves for the simulation cell size, reducing the number of waves calculated by a factor of f^2 . These plane waves are stored in realspace in a large array that we will refer to as the compact \mathbf{S} -matrix, with the output plane waves defined as $\mathbf{S}_{m,n}(\vec{r})$. These waves dimensions can be reduced by a factor of 4 if the multislice simulation used an anti-aliasing aperture position at half of the maximum scattering angle is used for the multislice simulations [18].

Next, we calculate each converged electron probe at position $\vec{r}_0 = (x_0, y_0)$ by first computing the required coefficients $\alpha_{m,n}(\vec{r}_0)$ for each plane wave $\mathbf{S}_{m,n}(\vec{r})$, and then multiplying these coefficients by the associated plane wave basis and summing over a sub-region centered around the probe. This is shown schematically in Fig. 1d. The sub-region is bounded by

$$\begin{aligned} x_0 - \frac{d}{2f} &\leq x < x_0 + \frac{d}{2f} \\ y_0 - \frac{d}{2f} &\leq y < y_0 + \frac{d}{2f}, \end{aligned} \quad (7)$$

giving a cutout region having an area of d^2/f^2 , which should be periodically wrapped around the simulation cell boundaries. The wave coefficients are defined as

$$\begin{aligned} \alpha_{m,n}(\vec{r}_0) &= A(\vec{q}) \exp[-i\chi(\vec{q})] \\ &\exp\{-2i\pi\vec{q}\cdot[x_0 - h\tan(\theta_x), \\ &y_0 - h\tan(\theta_y)]\}, \end{aligned} \quad (8)$$

where $A(\vec{q})$ is the probe aperture function defined as

$$A(\vec{q}) = \begin{cases} 1 & \text{where } |\vec{q}| \leq q_{\text{probe}} \\ 0 & \text{elsewhere.} \end{cases}$$

The probe can also contain coherent wave aberrations such as defocus C_1 or 3rd order spherical aberration C_3 described by the phase shift function [18]

$$\chi(\vec{q}) = \pi\lambda|\vec{q}|^2C_1 + \frac{\pi}{2}\lambda^3|\vec{q}|^4C_3 + \dots \quad (9)$$

Finally, the terms $h\tan(\theta_x)$ and $h\tan(\theta_y)$ shift the probe back to the center of a cutout region for a given simulation cell of height h and probe tilt angles θ_x and θ_y . As shown in Fig. 1e, once the probe coefficients $\alpha_{m,n}(\vec{r}_0)$ have been computed, the complex probe in realspace $\psi(\vec{r}, \vec{r}_0)$ can be computed using the summation

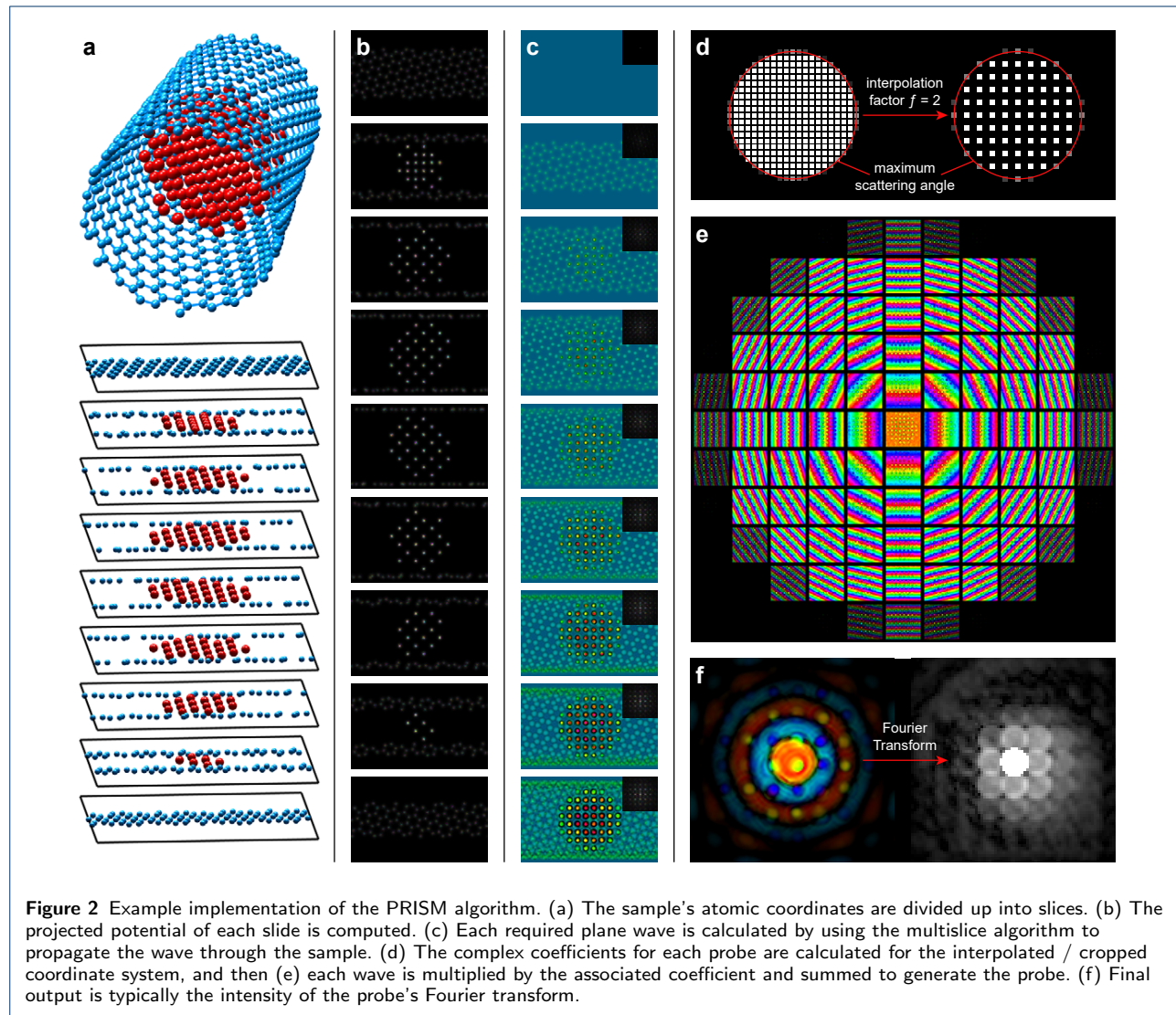
$$\psi(\vec{r}, \vec{r}_0) = \sum_{m,n} \mathbf{S}_{m,n}(\vec{r}) \alpha_{m,n}(\vec{r}_0), \quad (10)$$

in the cut out region defined by Eq. 7. Note that this expression is simply an expanded form of Eq. 2. Eq. 7 can be evaluated more quickly if we skip the addition of all terms where $\alpha_{m,n}(\vec{r}_0) = 0$. After the probe is computed we can either output the full probe diffraction pattern, or more commonly integrate a subset of the probe intensity after taking its Fourier transform, as in Fig. 1f. Once the output signals of all probes have been tabulated, the simulation is complete.

Simulation and Analysis Implementation

An implementation of the PRISM algorithm for a sample consisting of a nanoparticle contained within a carbon nanotube is shown in Figs. 2a-f. Each of the panels in this figure correspond to the same step as those given in Figs. 1a-f. In Figs. 2c, e and f, the wave phase is shown as the color hue, while the wave amplitude is shown by the brightness of each pixel.

All simulations and analysis in this study were performed using custom Matlab code. The multislice methods and the atomic potentials employed were taken from Kirkland [18]. We have included thermal scattering effects by using the frozen phonon approximation, which involves repeating the calculation with different phonon configurations (approximated with random atomic shifts) and summing the results incoherently.



Calculation Time for PRISM Simulations

We will now approximate the computation time of the PRISM algorithm, relative to traditional multislice simulations. We will neglect the computation time of the sample projected potential slices, as this calculation time is equal for both methods. We will also not consider thermal scattering, since it will require an increase in calculation time by an equal multiplier for both methods. For simplicity we will assume a square simulation cell with side length N where N is a power of two. Each slice will require the transmission and operations given in Eq. 5, which requires $6N \log_2(N)$ complex operations for the forward and inverse Fourier transforms and $2N^2$ operations to multiply the sample potential and the Fresnel propagation functions. If the entire STEM simulation consists of P unique probe positions and H slices through the sample, the total calculation time T_{multi} required is

$$\begin{aligned} T_{\text{multi}} &= HP [6N \log_2(N) + 2N^2] \\ &\approx 2HPN^2, \end{aligned} \quad (11)$$

if the simulation cell is large, i.e. $N \gg 1$. The PRISM method requires two parts to compute the scattering of all STEM probes. The first half of the algorithm requires B/f^2 multislice simulations, where B is the number of beams included in the full resolution simulation, which will be reduced by the interpolation factor squared. The second half is multiplication of the compact scattering matrix S for all beams (multislice plane waves computed in the previous step), which is required for P total probes, as in Eq. 10. This multiplication step is only required for the reduced number of beams B/f^2 , and the cut out region defined by Eq. 7 will reduce the number of multiplication operations to $N^2/4f^2$ (note the extra factor of 1/4 is due to storing only the part of S inside the anti-aliasing aperture). Therefore the total calculation time T_{PRISM} required for PRISM is

$$\begin{aligned} T_{\text{PRISM}} &= \frac{HB}{f^2} [6N \log_2(N) + 2N^2] + \frac{PBN^2}{4f^4} \\ &\approx BN^2 \left[\frac{2H}{f^2} + \frac{P}{4f^4} \right] \end{aligned} \quad (12)$$

Note that for a STEM probe, the probe amplitude coefficients beyond the probe semi-angle are zero and so the number of beams B used in practice is often much lower than the number of possible beams. The speedup offered by the PRISM algorithm is therefore approximately equal to the ratio of Eqs. 11 and 12, given by

$$\frac{T_{\text{Multi}}}{T_{\text{PRISM}}} = \frac{8HPf^4}{B(8Hf^2 + P)}. \quad (13)$$

Note that if the rate-limiting computation step for the PRISM algorithm is multiplying out the compact S -matrix, the speedup ratio does not depend on the number of probe positions P and the speedup will vary with f^4 . In the multislice and PRISM simulations given in the first results section below, the values of the terms of Eq. 13 were $H = 40$, $B \approx 10^4$ and $P \approx 10^5$. Plugging these numbers into Eq. 13 gives a speedup factor $T_{\text{Multi}}/T_{\text{PRISM}}$ of approximately 0.5, 8, 110 and 1100 for $f = 2, 4, 8$ and 16 respectively.

Results and Discussion

Comparison of Accuracy Between Multislice and PRISM

In general, PRISM will always be less accurate than corresponding multislice calculations, unless the PRISM speedup allows for finer pixel sampling or a similar effect. However the reduced accuracy is negligibly small in many cases, and will depend heavily on the microscope and sample parameters of a given simulation. To demonstrate this, we have compared the accuracy of a STEM probe calculation for a typical experimental geometry: a Pt nanoparticle approximately 7 nm diameter tilted 30° from the primary axis. It is resting upon an amorphous carbon substrate with a thickness of 5 nm, shown in Fig. 3a. The Pt nanoparticle has a multiply-twinned decahedral structure, with screw and edge dislocations present in two of the grains. The nanoparticle atomic coordinates were taken from [30], and the amorphous carbon structure was adapted from [31].

The sample was divided up into slices 0.2 nm thick, and the projected potential was computed for all slices. The sum of these potentials is shown in Fig. 3b, with an enlarged inset shown in Fig. 3d. The initial STEM probe generated from a 25 mrad semi-angle aperture at 80 kV is shown in Fig. 3c, with the probe center position shown in Fig. 3d. We then calculated the probe wavefunction after passing through the sample using the multislice method (Fig. 3e) and the PRISM algorithm with interpolation factors of $f = 2, 4, 8$ and 16 (Figs. 3f-i). The corresponding probe amplitudes in Fourier space are shown in Fig. 3j-n respectively, and the logarithm of the radially integrated intensities are plotted in Figs. 3o-s respectively. In the real space images, the channeling effect along aligned atomic columns is visible in all simulations [32].

We see that the PRISM method correctly reproduces most of the fine structure in the real space probe images. In Fig. 3i, we see that when $f = 16$ the tails of the probe have been cut off by the edge of the cropping window, leading to small artifacts at the boundary (shown with white arrows). However, Fig. 3n and

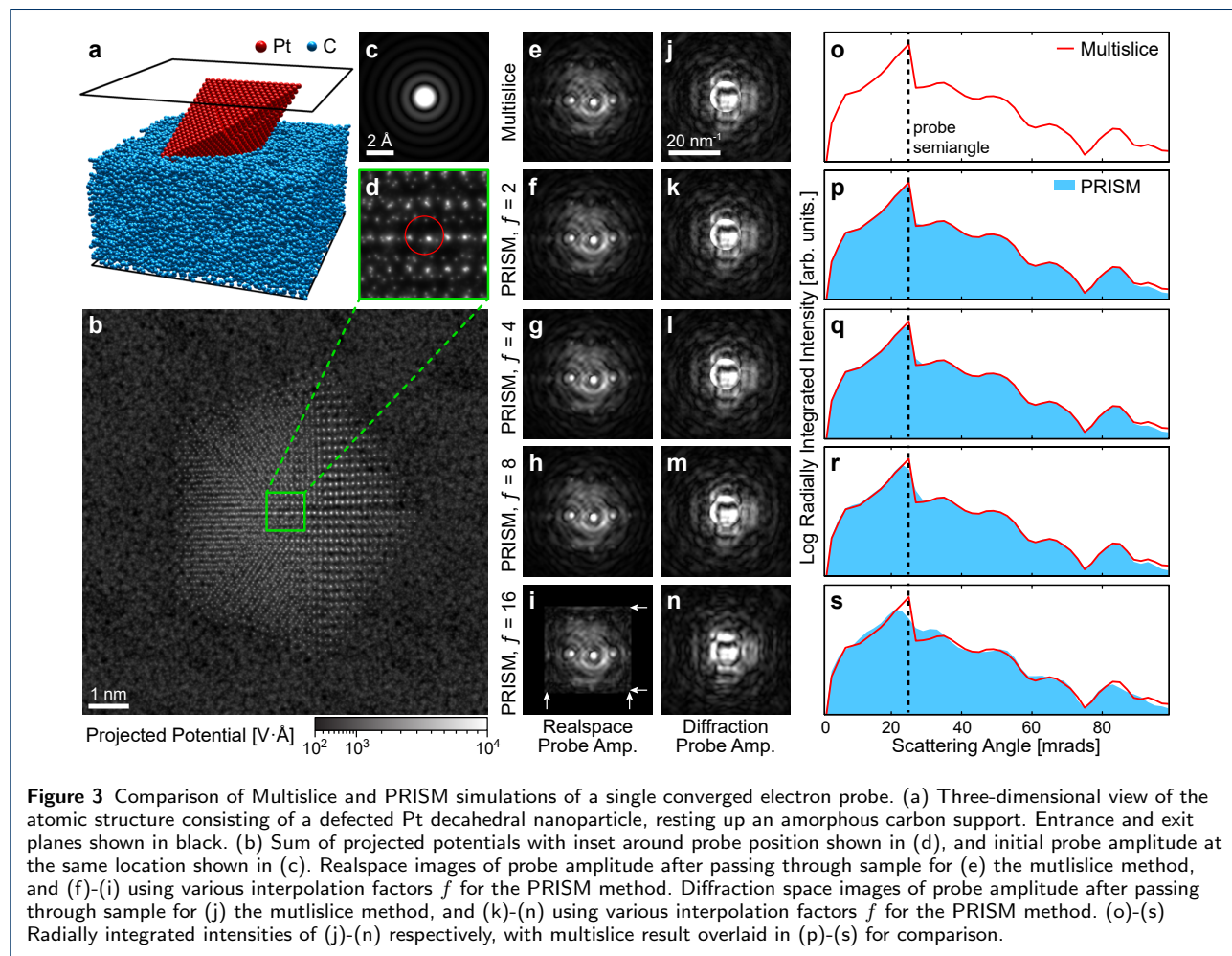


Fig. 3s show that this simulation can still qualitatively reproduce the diffracted probe signal with good accuracy. Overall, the only clearly visible difference in the PRISM simulations is the “blurring” effect caused by the Fourier interpolation, an effect which increases as f increases in Figs. 3k-n. This is reflected in the radially integrated intensities, as a small mixing between adjacent detector angle bins. We therefore conclude that PRISM is accurate enough to replace the traditional multislice method for STEM simulations in most cases. The primary exceptions are when the probe is very large (highly defocused or delocalized) or when fine details must be recovered from diffraction pattern, such as higher order Laue zone line measurements [33].

Varying Radial Detector Angles

HAADF With Varying Probe Size and Defocus

HAADF With Varying Beam Tilts

Conclusion

Acknowledgements

We thank Earl Kirkland, Christoph Koch and Roar Kilaas for helpful discussions. Work at the Molecular Foundry was supported by the Office of Science, Office of Basic Energy Sciences, of the U.S. Department of Energy under Contract No. DE-AC02-05CH11231.

References

1. Batson, P., Dellby, N., Krivanek, O.: Sub-ångstrom resolution using aberration corrected electron optics. *Nature* **418**(6898), 617–620 (2002)
2. Rose, H.: Prospects for aberration-free electron microscopy. *Ultramicroscopy* **103**(1), 1–6 (2005)
3. Dahmen, U., Erni, R., Radmilovic, V., Kselowski, C., Rossell, M.-D., Denes, P.: Background, status and future of the transmission electron aberration-corrected microscope project. *Philosophical Transactions of the Royal Society of London A: Mathematical, Physical and Engineering Sciences* **367**(1903), 3795–3808 (2009)
4. McMullan, G., Faruqi, A., Clare, D., Henderson, R.: Comparison of optimal performance at 300kev of three direct electron detectors for use in low dose electron microscopy. *Ultramicroscopy* **147**, 156–163 (2014)
5. Gautam, A., Ophus, C., Lançon, F., Denes, P., Dahmen, U.: Analysis of grain boundary dynamics using event detection and cumulative averaging. *Ultramicroscopy* **151**, 78–84 (2015)
6. Park, J., Elmlund, H., Ercius, P., Yuk, J.M., Limmer, D.T., Chen, Q., Kim, K., Han, S.H., Weitz, D.A., Zettl, A., et al.: 3d structure of individual nanocrystals in solution by electron microscopy. *Science* **349**(6245), 290–295 (2015)
7. Tate, M.W., Purohit, P., Chamberlain, D., Nguyen, K.X., Hovden, R., Chang, C.S., Deb, P., Turgut, E., Heron, J.T., Schlom, D.G., et al.: High dynamic range pixel array detector for scanning transmission electron microscopy. *Microscopy and Microanalysis* **22**(01), 237–249 (2016)
8. Li, X., Mooney, P., Zheng, S., Booth, C.R., Braufeld, M.B., Gubbens, S., Agard, D.A., Cheng, Y.: Electron counting and beam-induced motion correction enable near-atomic-resolution single-particle cryo-em. *Nature methods* **10**(6), 584–590 (2013)
9. Nogales, E.: The development of cryo-em into a mainstream structural biology technique. *Nature methods* **13**(1), 24–27 (2016)
10. Glaeser, R.M.: How good can cryo-em become? *Nature methods* **13**(1), 28–32 (2016)
11. Ophus, C., Ercius, P., Sarahan, M., Czarnik, C., Ciston, J.: Recording and using 4d-stem datasets in materials science. *Microscopy and Microanalysis* **20**(S3), 62–63 (2014)
12. Ozdal, V., Gammer, C., Jin, X., Ercius, P., Ophus, C., Ciston, J., Minor, A.: Strain mapping at nanometer resolution using advanced nano-beam electron diffraction. *Applied Physics Letters* **106**(25), 253107 (2015)
13. Pekin, T.C., Gammer, C., Ciston, J., Minor, A.M., Ophus, C.: Optimizing disk registration algorithms for nanobeam electron diffraction strain mapping. *Submitted to Ultramicroscopy* (2017)
14. Panova, O., Chen, X.C., Bustillo, K.C., Ophus, C., Bhatt, M.P., Balsara, N., Minor, A.M.: Orientation mapping of semicrystalline polymers using scanning electron nanobeam diffraction. *Micron* **88**, 30–36 (2016)
15. Shibata, N., Findlay, S.D., Kohno, Y., Sawada, H., Kondo, Y., Ikuhara, Y.: Differential phase-contrast microscopy at atomic resolution. *Nature Physics* **8**(8), 611–615 (2012)
16. Ophus, C., Ciston, J., Pierce, J., Harvey, T.R., Chess, J., McMoran, B.J., Czarnik, C., Rose, H.H., Ercius, P.: Efficient linear phase contrast in scanning transmission electron microscopy with matched illumination and detector interferometry. *Nature communications* **7** (2016)
17. Yang, H., Rutte, R., Jones, L., Simson, M., Sagawa, R., Ryll, H., Huth, M., Pennycook, T., Green, M., Soltau, H., et al.: Simultaneous atomic-resolution electron ptychography and z-contrast imaging of light and heavy elements in complex nanostructures. *Nature Communications* **7** (2016)
18. Kirkland, E.: Advanced computing in electron microscopy (2010)
19. Bethe, H.: Theorie der beugung von elektronen an kristallen. *Annalen der Physik* **392**(17), 55–129 (1928)
20. Zuo, J., Spence, J.: *Electron Microdiffraction*. Springer, ??? (2013)
21. Cowley, J.M., Moodie, A.F.: The scattering of electrons by atoms and crystals. i. a new theoretical approach. *Acta Crystallographica* **10**(10), 609–619 (1957)
22. Shukla, A.K., Ramasse, Q.M., Ophus, C., Duncan, H., Hage, F., Chen, G.: Unravelling structural ambiguities in lithium-and manganese-rich transition metal oxides. *Nature Communications* **6** (2015)
23. Van den Broek, W., Jiang, X., Koch, C.: FDES, a GPU-based multislice algorithm with increased efficiency of the computation of the projected potential. *Ultramicroscopy* **158**, 89–97 (2015)
24. Xu, R., Chen, C.-C., Wu, L., Scott, M., Theis, W., Ophus, C., Bartels, M., Yang, Y., Ramezani-Dakhel, H., Sawaya, M.R., et al.: Three-dimensional coordinates of individual atoms in materials revealed by electron tomography. *Nature materials* **14**(11), 1099–1103 (2015)
25. Yang, Y., Chen, C.-C., Scott, M., Ophus, C., Xu, R., Pryor Jr, A., Wu, L., Sun, F., Theis, W., Zhou, J., et al.: Deciphering chemical order/disorder and material properties at the single-atom level. *arXiv preprint arXiv:1607.02051* (2016)
26. Grillo, V., Rotunno, E.: Stem_cell: A software tool for electron microscopy: Part i—simulations. *Ultramicroscopy* **125**, 97–111 (2013)
27. Allen, L., Findlay, S., et al.: Modelling the inelastic scattering of fast electrons. *Ultramicroscopy* **151**, 11–22 (2015)
28. Hosokawa, F., Shinkawa, T., Arai, Y., Sannomiya, T.: Benchmark test of accelerated multi-slice simulation by gppgpu. *Ultramicroscopy* **158**, 56–64 (2015)
29. Lobato, I., Van Aert, S., Verbeeck, J.: Progress and new advances in simulating electron microscopy datasets using multem. *Ultramicroscopy* (2016)
30. Chen, C.-C., Zhu, C., White, E.R., Chiu, C.-Y., Scott, M., Regan, B., Marks, L.D., Huang, Y., Miao, J.: Three-dimensional imaging of dislocations in a nanoparticle at atomic resolution. *Nature* **496**(7443), 74–77 (2013)
31. Ricolleau, C., Le Bouar, Y., Amara, H., Landon-Cardinal, O., Alloyeau, D.: Random vs realistic amorphous carbon models for high resolution microscopy and electron diffraction. *Journal of Applied Physics* **114**(21), 213504 (2013)
32. Pennycook, S.J., Nellist, P.: Scanning transmission electron microscopy: imaging and analysis (2011)
33. Jones, P., Rackham, G., Steeds, J.: Higher order laue zone effects in

electron diffraction and their use in lattice parameter determination.
In: Proceedings of the Royal Society of London A: Mathematical,
Physical and Engineering Sciences, vol. 354, pp. 197–222 (1977)